Extraction of alumina and silica from high-silica bauxite by sintering with sodium carbonate followed by two-step leaching with water and sulfuric acid

Yue Sun, [ID] [a] Aifang Pan, [ID] *[ab] Yuzhao Ma*[c] and Jie Chang[c]

Efficient utilization of high-silica bauxite and minimization of bauxite residue are of great significance for the sustainable development of the alumina industry. In this paper, a novel process is proposed to extract Al_2O_3 and SiO_2 from high-silica bauxite without residue discharge, that is, sintering bauxite with Na_2CO_3 followed by two-step leaching with water and sulfuric acid. The effects of the sintering parameters on the process were investigated, and the phase transformations during sintering and leaching were revealed by using phase diagram, thermogravimetric analysis (TGA) and differential scanning calorimetric (DSC), X-ray diffraction (XRD), scanning electron microscopy (SEM) and energy dispersive spectrometer (EDS) methods. When the mixture of the high-silica bauxite and Na_2CO_3 with mole ratio of $Na_2O/(Al_2O_3 + SiO_2)$ of 1 was sintered at 950 °C for 30 min, diaspore and kaolinite were primarily converted into $Na_{1.95}Al_{1.95}Si_{0.05}O_4$ and an amorphous phase, respectively. In the water leaching process, $Na_{1.95}Al_{1.95}Si_{0.05}O_4$ was dissolved while the amorphous phase underwent some transformations to form the water leaching residue, resulting in ~84% of Al_2O_3 being extracted for alumina production. In the sulfuric acid leaching process, the amorphous phase in the water leaching residue dissolved, resulting in ~13% of Al_2O_3 and ~86% of SiO_2 being extracted for the production of polyaluminium ferric sulfate (PAFS) and silica gel, respectively. The silica gel had a high purity, containing more than 88% of SiO_2 after drying.

1 Introduction

Silica is a major impurity in bauxite ores, which is commonly present as quartz (SiO_2) and phyllosilicate minerals such as kaolinite ($Al_4[Si_4O_{10}](OH)_8$), illite ($K_xAl_4Si_{8-x}Al_xO_{20}(OH)_2$) and pyrophyllite ($Al_2[Si_4O_{10}](OH)_2$).[1,2] When producing alumina from bauxite using the Bayer process, the reactive silica is transformed into insoluble sodium aluminosilicate hydrate known as desilication product (DSP), resulting in a severe loss of alumina and caustic soda.[3–5] As a result, high-silica bauxite, in which reactive silica is above ~8%, cannot be economically processed by the conventional Bayer process.[2] With the increase of alumina production, high-grade bauxite is rapidly consumed, leading to an increase in the proportion of high-silica bauxite. Efficient development and utilization of high-silica bauxite has become an urgent and significant challenge for the alumina industry.

[a]School of Earth Science and Resources, Chang'an University, Xi'an 710054, China. E-mail: panaifang@126.com

[b]Institute for Interdisciplinary and Innovate Research, Xi'an University of Architecture and Technology, Xi'an 710055, China

[c]College of Materials Science and Engineering, Xi'an University of Architecture and Technology, Xi'an 710055, China. E-mail: yuzhaoma@126.com

Many methods have been developed to extract alumina from high-silica bauxite, which can be broadly classified into four main categories, as shown in Table 1. Among these methods, most are at the experimental stage and only a few have been applied industrially. The flotation-Bayer process has been widely applied in the alumina refineries, but it introduces large amounts of hazardous organic reagents and produces tailings totaling of about 25% of the initial bauxite ores in weight.[25,26] The lime Bayer process has been also employed to process a portion of high-silica bauxite, but it cannot economically process the bauxite with a mass ratio of alumina to silica (A/S) lower than 5.[7] For processing high-silica bauxites with A/S < 5, the lime-soda sintering process and its various combinations with the Bayer process are the preferred choice.[27] However, they are barely economically viable due to the high operating costs. In addition, the extraction of silica is rarely considered by the methods listed in Table 1. Only in the chemical beneficiation of high-silica bauxite, silica is extracted into alkali solutions and is used to produce silicate products such as 4A zeolite.[28,29] In other methods, silica is left in the bauxite residue.

Bauxite residue is a solid waste left over after extracting alumina from bauxite. When high-silica bauxite is used as

Table 1 Classification of methods for processing high-silica bauxite

Category	Description	Limitation	Method	Development stage
Pre-desilication of high-silica bauxite followed by the Bayer process	Improving the A/S of high-silica bauxite by physical, chemical and biological beneficiation methods to meet the requirement of the Bayer process	Physical beneficiation discharges a lot of tailings, wasting serious resources. Chemical beneficiation is difficult in recycling desilication solutions and high in production costs. Biological beneficiation has a long processing period and an unstable desilication efficiency	Flotation[6]	Industrial application
			Alkali leaching[7]	Experimental stage
			Roasting-alkali leaching[8]	Experimental stage
			Reduction roasting-alkali leaching[9]	Experimental stage
			Biological desilication[10]	Experimental stage
The Bayer process variations	Converting the reactive silica into hydrogarnet or calcium silicate by adding lime and adjusting digestion conditions, resulting in a lower loss of caustic soda	Adding large amount of lime increases the burden of solid–liquid separation and the sodium carbonate content in sodium aluminate solution. Increasing alkali concentration leads to a difficult solid–liquid separation and a greater evaporation energy consumption	The lime Bayer process[11]	Industrial application
			The calcification–carbonization process[12]	Experimental stage
			The hydro-chemical process[13]	Experimental stage
			The sub-molten salt process[14]	Experimental stage
Sintering processes	Converting silica into insoluble dicalcium silicate during sintering and separating it with soluble sodium (or calcium) aluminate during leaching	Sintering processes are high in energy consumption and poor in economic efficiency	The lime-soda sintering process[15]	Industrial application
			The lime-soda sintering process variations[16,17]	Experimental stage
			The lime sintering process[18]	Stop production after application
Acid methods	Processing bauxite with acid or ammonium salt to get aluminum salt solution and leaving silica in the residue	Acid has a serious corrosion on equipment, while ammonium salt has a potential ammonia leak. In addition, impurities in aluminum salt solutions are difficult and costly to remove	Ammonium sulfate roasting-water leaching[19,20]	Experimental stage
			Acid leaching[21–23]	Experimental stage
			Thermal or mechanical activation-acid leaching[24]	Experimental stage

a feedstock for alumina production, more bauxite residue is discharged compared to processing high-grade bauxite.[30] At present, most bauxite residues are sent to dams for storage, taking up large amounts of land and incurring significant costs for the construction and maintenance of the dams.[31,32] In addition, long-time storage of bauxite residue poses a potential threat to the surrounding environment and may cause safety accidents such as leakage and dam failure.[33] Therefore, minimization and recycling of bauxite residue should be considered in the production of alumina. However, the alkali methods listed in Table 1 rarely take this aspect into account. Only the calcification–carbonization process proposed to recycle bauxite residue for preparing cement.[34] Compared with the alkali methods, the acid methods produce less residue which is highly enriched in silica and can be used as a raw material for inorganic silica products.[19,23]

Alkali methods are well established in the production of alumina, while acid methods have advantages in the minimization and recycling of bauxite residue. Therefore, an attempt can be made to combine the alkali and acid methods.

In our previous studies, a novel combined alkali-acid process was proposed to extract aluminum, silicon and iron from silver tailings.[35,36] In the present study, the process was adapted to realize the extraction of Al_2O_3 and SiO_2 from high-silica bauxite without residue discharge, as shown in Fig. 1. First, high-silica bauxite is activated by sintering with Na_2CO_3. Second, water leaching is conducted at atmospheric pressure to extract most of Al_2O_3 from the sintered sample into the sodium aluminate solution, which can be used to produce alumina by desilication, carbonation decomposition and calcination. Third, sulfuric acid leaching is conducted at atmospheric pressure to extract SiO_2 and the remaining Al_2O_3 from the water leaching residue into the acid leaching solution, which can be used to produce silica gel and poly-aluminium ferric sulfate (PAFS) by aging, separation, concentration and polymerization. This study aims to investigate the effects of sintering temperature (850–1050 °C), sintering time (10–50 min) and the mole ratio of $Na_2O/(Al_2O_3 + SiO_2)$ (0.6–1.4) on the extraction of Al_2O_3 and SiO_2, and to reveal the process mechanism using phase diagram,
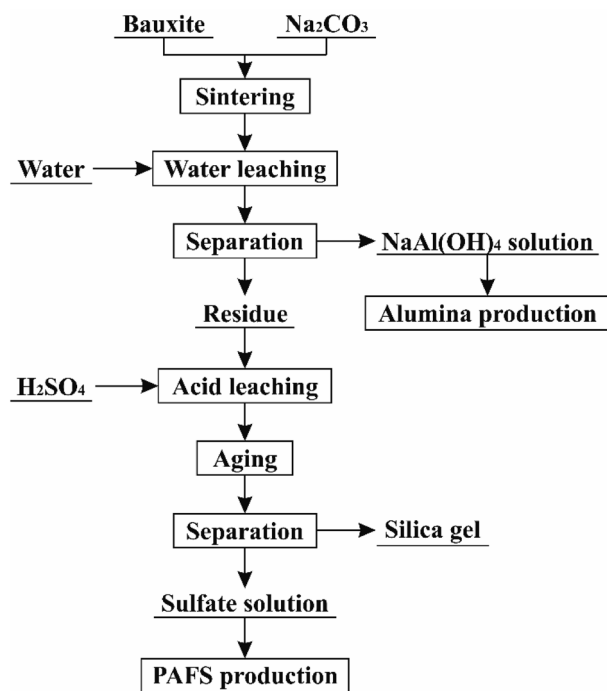
Fig. 1 Flowsheet for extraction of alumina and silica from high-silica bauxite.

thermogravimetric analysis (TGA) and differential scanning calorimetric (DSC), X-ray diffraction (XRD), scanning electron microscope (SEM) and energy dispersive spectrometer (EDS) techniques.

2 Experimental

2.1 Raw materials

The high-silica bauxite sample used in this study had been described in our previous study, which has a high Al_2O_3 content of 62.92%, a high SiO_2 content of 16.72%, a low A/S of 3.76, and a mineral composition (Fig. 2(a)) dominated by diaspore (63.4%) and kaolinite (31.2%).[37] The particle size distribution (Fig. 2(b)) of the high-silica bauxite indicates that 80% of the particles are distributed in the range of 3.15–21.74 μm with a D50 value of 9.48 μm. The SEM images (Fig. 2(c) and (d)) and EDS results (Table 2) of the high-silica bauxite indicate that diaspore particles are primarily in massive and slaty structure, while kaolinite particles are primarily in layer structure. The particle distribution and morphological characteristics of the high-silica bauxite favor its sintering reaction with Na_2CO_3.

All the chemical reagents used in the study are analytically pure. The concentration of concentrated sulfuric acid is 18 mol L^{-1}, which was diluted with distilled water to the specified concentration.

2.2 Methods and processes

The high-silica bauxite was mixed evenly with various amounts of Na_2CO_3 in a ceramic mortar. The mixtures were transferred to a muffle furnace and sintered for a certain time after the temperature is raised to a specified level. The sintered samples were cooled to room temperature and then ground to below 74 μm in particle size for leaching. The experimental ranges of Na_2CO_3 dosage, sintering temperature and sintering time were
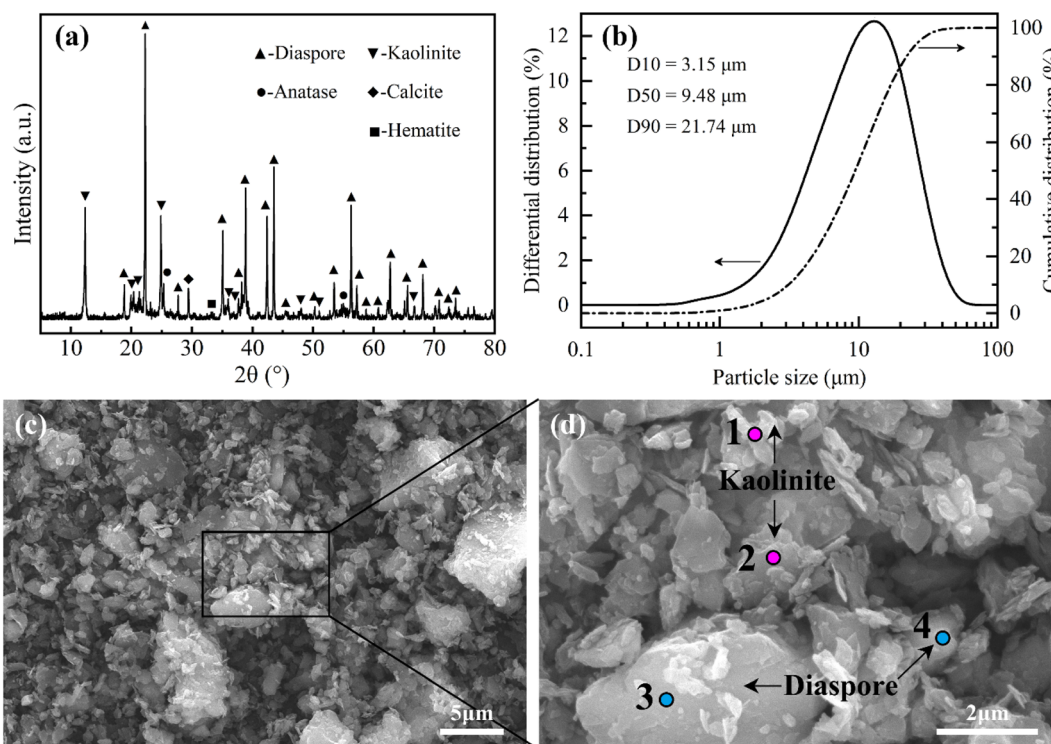

Fig. 2 Characterizations of the high-silica bauxite: (a) XRD pattern; (b) particle size distribution; (c and d) SEM images.

Table 2 Elemental compositions of bauxite particles from EDS analysis (wt%)

Element	O	Al	Si	Ca	Ti	Fe
Spot 1	54.27	25.20	17.86	—	1.56	1.11
Spot 2	51.06	27.13	19.55	—	0.71	1.55
Spot 3	53.36	41.46	3.38	—	0.66	1.24
Spot 4	46.03	43.19	4.86	3.37	1.22	1.33
Average	51.18	34.25	11.41	0.84	1.04	1.31

determined by phase diagram calculation, simultaneous thermal analysis and previous experience, respectively.

The sintered samples were leached in distilled water at 75 °C for 15 min with a solid/liquid ratio of 1 g/15 mL. Water leaching residues were separated from the slurries, washed five times with hot distilled water, and then dried at 105 °C for 2 h. The dry residues were leached in a 2 mol L^{-1} sulfuric acid solution at room temperature for 10 min with a solid/liquid ratio of 1 g/10 mL. After acid leaching, no solid–liquid separation was performed. The acid leaching solutions were aged at 85 °C for 1.5 h to precipitate silica gel, which was subsequently separated and washed with hot distilled water until neutral. The silica gels were dried at 110 °C for 12 h to obtained silica powders.

The contents of Al_2O_3 and SiO_2 in solid samples were analyzed by complexometric titration and spectrophotometry (or hydrofluoric acid gravimetry), respectively. The recovery efficiencies of Al_2O_3 and SiO_2 were calculated according to the following equations.

$$\eta_{A1} = [1 - (c_{A2}/c_{S2})/(c_{A1}/c_{S1})] \times 100\% \tag{1}$$

$$\eta_{A2} = (m_2 \times c_{A2} - m_3 \times c_{A3})/(m_1 \times c_{A1}) \times 100\% \tag{2}$$

$$\eta_{AT} = \eta_{A1} + \eta_{A2} \tag{3}$$

$$\eta_S = m_3 \times c_{S3}/(m_1 \times c_{S1}) \times 100\% \tag{4}$$

where η_{A1}, η_{A2} and η_{AT} represent the recovery efficiencies of Al_2O_3 in water leaching, acid leaching and total process, respectively, η_S represent the recovery efficiency of SiO_2, m_1, m_2 and m_3 are the masses of sintered sample, water leaching residue and silica powder, respectively (g), c_{A1}, c_{A2} and c_{A3} are the contents of Al_2O_3 in sintered sample, water leaching residue and silica powder, respectively (%), and c_{S1}, c_{S2} and c_{S3} are the contents of SiO_2 in sintered sample, water leaching residue and silica powder, respectively (%).

2.3 Characterizations of solid samples

Particle size distribution was analyzed by a Bettersize 2000 laser particle size analyzer. Chemical compositions were determined by a Shimadzu 1800 X-ray fluorescence (XRF) spectrometer. X-ray diffraction (XRD) patterns were recorded on a Rigaku D/MAX 2000 X-ray diffractometer and the mineral compositions were identified using the Jade software. Thermo-gravimetric analysis (TGA) and differential scanning calorimetric (DSC) were performed using a Mettler Toledo 1/1600 simultaneous thermal analyzer at a heating rate of 10 °C min^{-1} in a nitrogen atmosphere. The micromorphology and element distribution were conducted by a scanning electron microscopy equipped
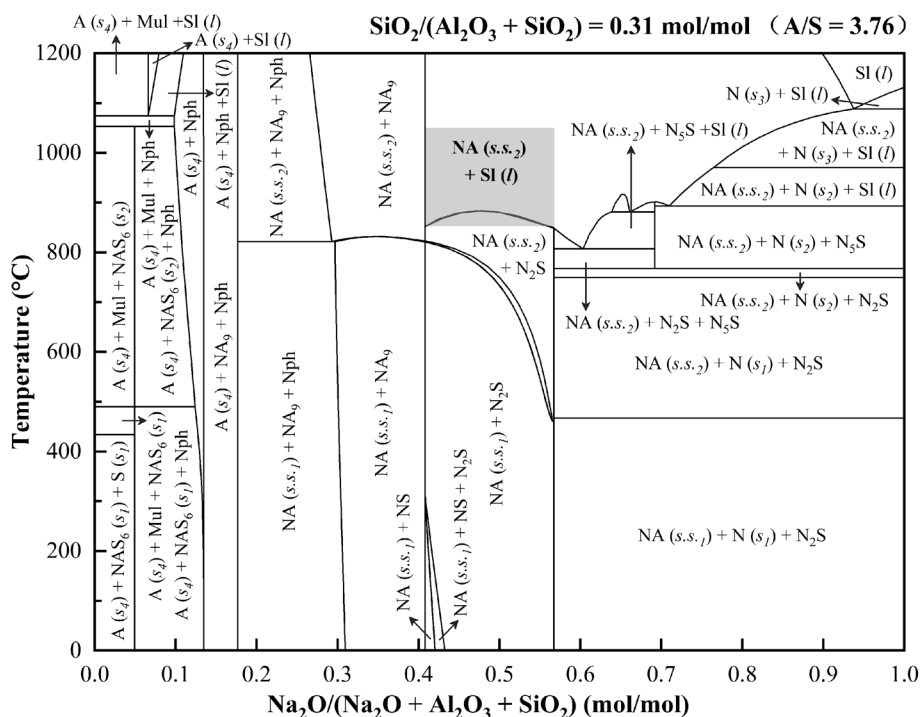

Fig. 3 Calculated phase diagram of the Na_2O–Al_2O_3–SiO_2 system (A – Al_2O_3, N – Na_2O, S – SiO_2, NA – $NaAlO_2$, NA_9 – $NaAl_9O_{14}$, NS – Na_2SiO_3, N_2S – Na_4SiO_4, N_5S – $Na_{10}SiO_7$, NAS_6 – $NaAlSi_3O_8$, Mul – mullite, Nph – nepheline, Sl – slag, s – solid, l – liquid, s.s. – solid solution).
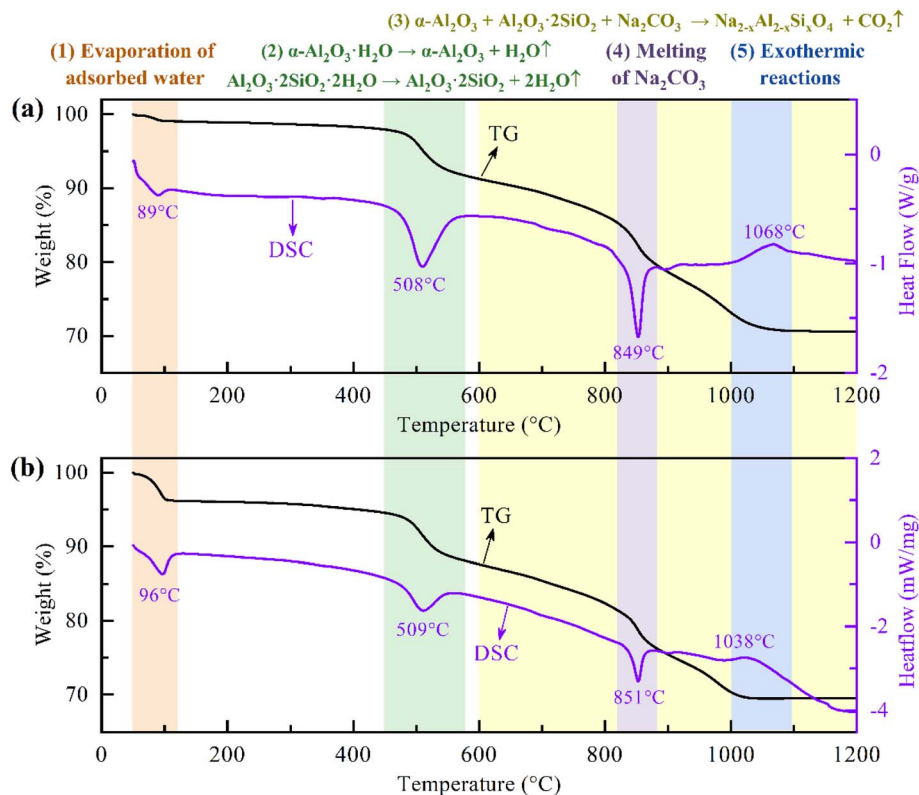
Fig. 4 TG and DSC curves of the mixture of bauxite and Na_2CO_3 with N/(A + S) = 1 under nitrogen (a) and air (b)[37] atmospheres.

with energy disperse X-ray spectrometry (MLA650F, F.E.I.). Specific surface area was analyzed by a Brunauer–Emmett–Teller (BET) surface area analyzer (Nova Station A, Quantachrome).

3   Results and discussion

3.1   Setting of experimental parameters

In the sintering process, Na_2CO_3 dosage, sintering temperature and sintering time are the key parameters affecting the extraction of Al_2O_3 and SiO_2. A theoretical analysis must be performed to rationalize the experimental range of these parameters.

The dosages of sintering additives are usually determined by the contents of the major components in bauxite. In the traditional lime-soda sintering process, the dosages of Na_2CO_3 and CaO are controlled by the molar ratios of $Na_2O/Al_2O_3 \approx 1$ and $CaO/SiO_2 \approx 2$ to ensure the formations of $NaAlO_2$ and Ca_2SiO_4, respectively.[16,38] In this study, both Al_2O_3 and SiO_2 would react with Na_2CO_3 due to the absence of CaO. Therefore, the molar
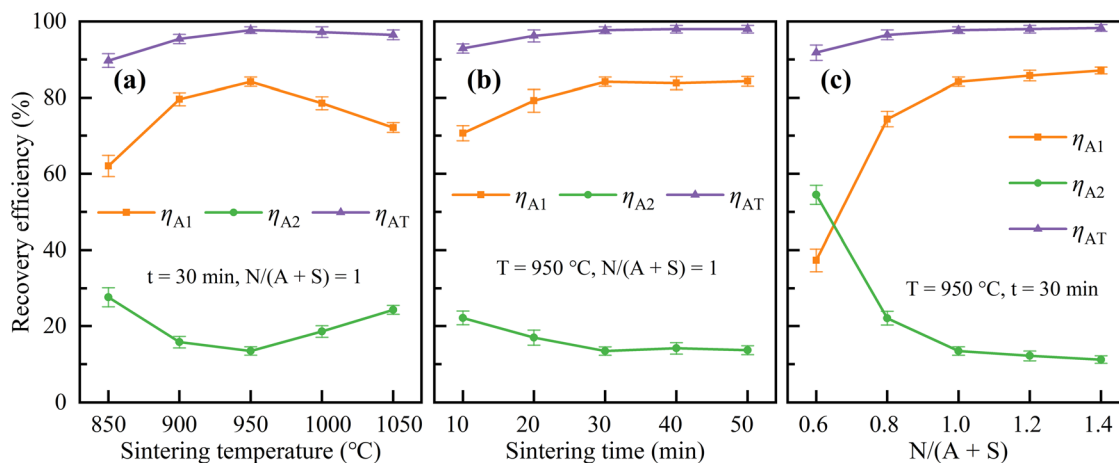

Fig. 5 Effects of sintering temperature (a), sintering time (b), and N/(A + S) (c) on the recovery efficiencies of Al_2O_3.
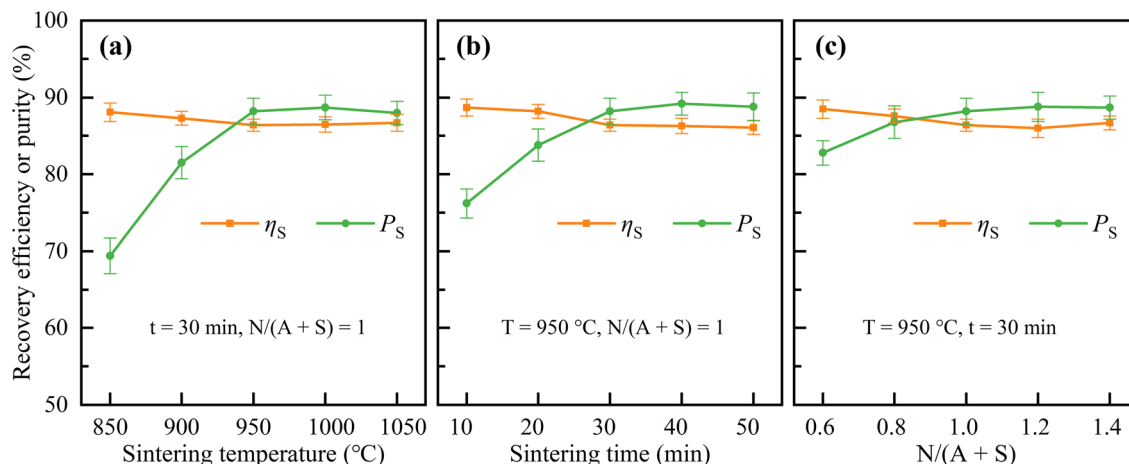
Fig. 6 Effects of sintering temperature (a), sintering time (b), and N/(A + S) (c) on the recovery efficiency of SiO_2 and the purity of silica powder.

ratio of $Na_2O/(Al_2O_3 + SiO_2)$ (N/(A + S)) should be used as the indicator for controlling Na_2CO_3 dosage.

Phase diagram calculations are generally used to model the equilibrium behavior of multi-component systems at various compositions and temperatures.[39] The experimental range of N/(A + S) could be determined by analyzing the equilibrium phase changes in the $Na_2O–Al_2O_3–SiO_2$ system. The phase diagram of the $Na_2O–Al_2O_3–SiO_2$ system was calculated using the phase diagram module of FactSage software based on the FACT oxide compounds and solutions (FToxid) databases, as shown in Fig. 3. When the mole fraction of Na_2O is less than 0.41, Al_2O_3, SiO_2 or $NaAl_9O_{14}$ appear as stable phases, indicating that Na_2O is insufficient to fully react with Al_2O_3 and SiO_2. When the mole fraction of Na_2O is above 0.57, Na_2O is present as one of the stable phases, indicating its excess in the system. As the mole fraction of Na_2O is in the range of 0.41–0.57, the stable phases are $NaAlO_2$ solid solution coupled with Na_2SiO_3, Na_4SiO_4 or a liquid slag. Among them, $NaAlO_2$ solid solution is the effective phase for alumina extraction. Therefore, it is more appropriate for the mole fraction of Na_2O between 0.41–0.57, which is converted to N/(A + S) of 0.69–1.33. Considering that minor amounts of Fe_2O_3, TiO_2 and other components in bauxite would have a certain influence on Na_2CO_3 dosage, the experimental range of N/(A + S) was extended to 0.6–1.4 in this study.

In order to determine the experimental range of sintering temperature, the thermal behavior of the mixture of bauxite and Na_2CO_3 with N/(A + S) = 1 during heating was analyzed by TGA/DSC under a nitrogen atmosphere, as shown in Fig. 4(a).

There were three endothermic peaks at 89 °C, 508 °C and 849 °C, and one exothermic peak at 1068 °C on the DSC curve. The endothermic peaks at 89 °C and 508 °C were primarily attributed to the removal of adsorbed water and structural water, respectively. Accordingly, significant weight losses were observed around 89 °C and 508 °C on the TG curves. After removing the structural water, diaspore (α-$Al_2O_3 \cdot H_2O$) and kaolinite ($Al_2O_3 \cdot 2SiO_2 \cdot 2H_2O$) were transformed into alpha-alumina (α-Al_2O_3) and metakaolinite ($Al_2O_3 \cdot 2SiO_2$), respectively, which can further react with Na_2CO_3 to form $NaAlO_2$ solid solutions ($Na_{2-x}Al_{2-x}Si_xO_4$, $x \leq 0.55$) eventually.[37] Therefore, the weight loss in the TG curve above 600 °C was primarily attributed to the release of CO_2 from the reaction between bauxite and Na_2CO_3. The third endothermic peak was located at about 849 °C, where the melting of Na_2CO_3 significantly increased the reaction rate between bauxite and Na_2CO_3,[40] resulting in a significant increase in the weight loss rate of the TG curve. Thus, the sintering temperature should be set above 849 °C to improve the sintering efficiency and shorten the sintering time. The TG curve was no longer significantly losing weight upon reaching a temperature of about 1050 °C, indicating that Na_2CO_3 was fully involved in the reaction with bauxite. Therefore, the experimental upper limit of the sintering temperature could be set at 1050 °C. In summary, the range of sintering temperature investigated in this study was set as 850–1050 °C. According to Fig. 3, the stable phases at 850–1050 °C were primarily $NaAlO_2$ solid solution and a liquid slag. The exothermic peak at 1068 °C indicated that some exothermic

Table 3 Chemical composition of the solid samples obtained at optimal sintering parameters (wt%)

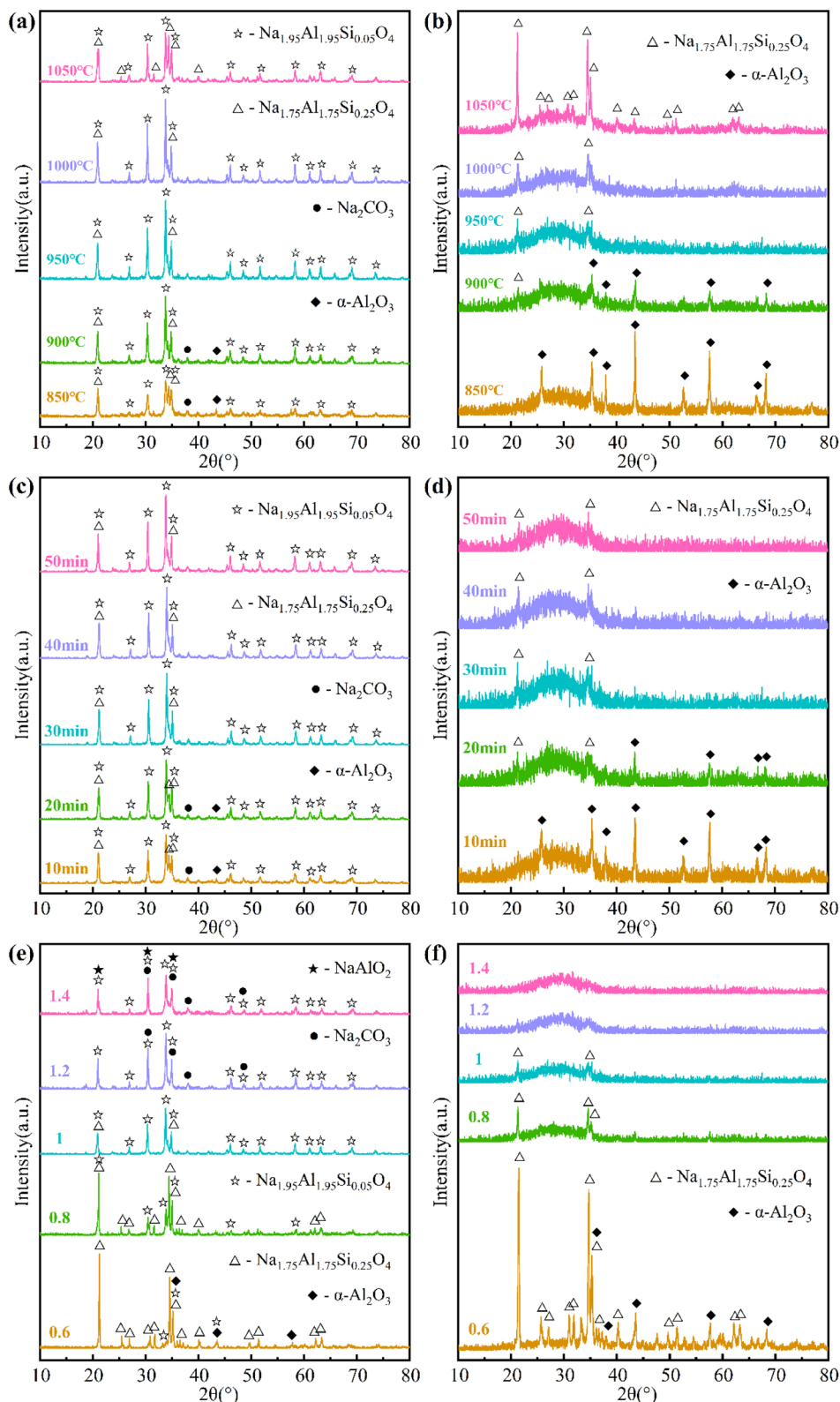| Component	Al_2O_3	SiO_2	Fe_2O_3	CaO	Na_2O	TiO_2	LOI
Sintered sample	42.3 ± 1.0	11.4 ± 0.4	2.7 ± 0.2	0.6 ± 0.1	39.2 ± 0.8	1.6 ± 0.1	1.7 ± 0.3
Water leaching residue	20.0 ± 0.6	34.4 ± 0.9	9.5 ± 0.3	2.3 ± 0.1	9.2 ± 0.5	5.5 ± 0.3	16.2 ± 1.9
Silica powder	1.1 ± 0.2	88.2 ± 1.7	0.6 ± 0.2	0.5 ± 0.1	0.6 ± 0.1	2.6 ± 0.3	6.5 ± 1.5

Fig. 7 XRD patterns of sintered samples (a, c and e) and water leaching residues (b, d and f).

reactions occurred in the temperature range of 1000–1100 °C. In addition, the TGA/DSC results under nitrogen atmosphere are highly similar to those under air atmosphere (Fig. 4(b)) that we studied previously,[37] indicating that different

atmospheres and variable oxygen exposure have no obvious impact on the sintering process.

The sintering time depends on the reaction rate, which in turn depends on the sintering temperature. In our previous studies, the
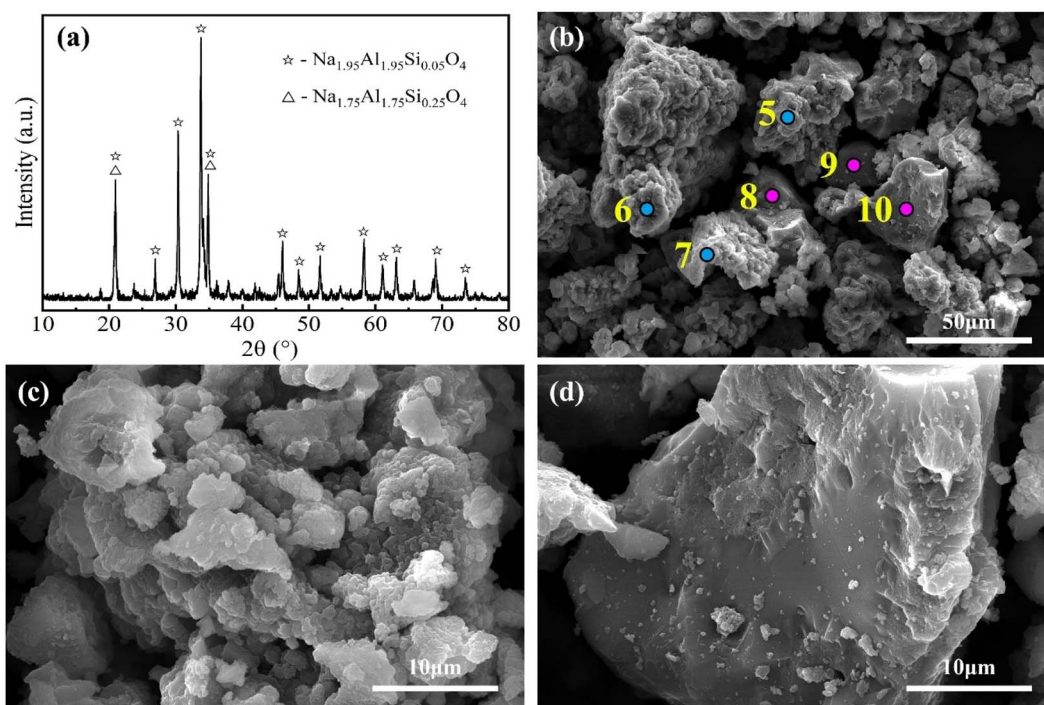
Fig. 8 XRD pattern (a) and SEM images (b–d) of the sintered sample obtained at optimal sintering parameters.

Table 4 Elemental compositions of the sintered sample particles from EDS analysis (wt%)

Element	O	Na	Al	Si	Ca	Ti	Fe
Spot 5	33.82	31.52	27.02	5.68	0	0.64	1.32
Spot 6	22.81	32.3	31.2	6.42	0	3.53	3.74
Spot 7	32.39	36.3	18.09	3.82	0.38	0.48	1.21
Average (5–7)	29.67	33.37	25.44	5.31	0.13	1.55	2.09
Standard deviation	5.99	2.56	6.70	1.34	0.22	1.72	1.43
Spot 8	33.83	26.88	16.52	5.32	0.36	1.31	3.71
Spot 9	34.11	29.02	14.93	4.94	0.78	1.63	3.44
Spot 10	33.36	32.71	15.04	5.45	1	3.99	8.45
Average (8–10)	33.77	29.54	15.50	5.24	0.71	2.31	5.20
Standard deviation	0.38	2.95	0.89	0.27	0.33	1.46	2.82

sintering time was usually set to 30 min.[36,37] In this study, the experimental range of sintering time was set to 10–50 min.

3.2 Effects of sintering parameters on the extraction of alumina and silica

The effects of sintering temperature, sintering time, and $N/(A + S)$ on the extraction of Al_2O_3 and SiO_2 were investigated sequentially according to the set experimental ranges, and the results were shown in Fig. 5 and 6.

As shown in Fig. 5, the sintering parameters have a significant impact on the recovery efficiencies of Al_2O_3. Under the conditions of $N/(A + S) = 1$ and a sintering time of 30 min, the recovery efficiency of Al_2O_3 in water leaching process (η_{A1}) was first increased and then decreased when the sintering temperature was increased from 850 °C to 1050 °C

and reached a maximum value of 84.2% at 950 °C. Under the conditions of $N/(A + S) = 1$ and a sintering temperature of 950 °C, η_{A1} increased significantly when the sintering time was prolonged from 10 min to 30 min. Upon further prolonging the sintering time to 50 min, η_{A1} was stabilized at about 84%. Under the conditions of a sintering temperature of 950 °C and a sintering time of 30 min, η_{A1} continued to increase from 37.3% to 87.1% when $N/(A + S)$ was increased from 0.6 to 1.4, and the increase became gradually lower. The recovery efficiency of Al_2O_3 in acid leaching process (η_{A2}) showed an opposite trend to that of η_{A1}, while the total recovery efficiency of Al_2O_3 (η_{AT}) showed a similar trend to that of η_{A1} with lower rangeability. η_{AT} was maintained above 90%, up to 98.3%.

As shown in Fig. 6, the sintering parameters had little effect on the recovery efficiency of SiO_2 (η_S), but had a significant effect on the purity of silica powder (P_S). η_S was mainly distributed in the range of 85–89% with slight variations. Silica powder had a high purity of 87–90% under the conditions of sintering temperature of 950–1050 °C, sintering time of 30–50 min or $N/(A + S) = 1$–1.4. But under other conditions, the purity of silica powder was lower.

According to the above experimental results, the optimal sintering parameters were selected as sintering temperature of 950 °C, sintering time of 30 min and $N/(A + S) = 1$. Under these conditions, η_{A1}, η_{A2}, η_{AT}, and η_S were 84.2%, 13.5%, 97.7% and 86.4%, respectively. The silica powder obtained at optimal sintering parameters had a purity of 88.2%. The chemical compositions of the corresponding solid samples are shown in Table 3.
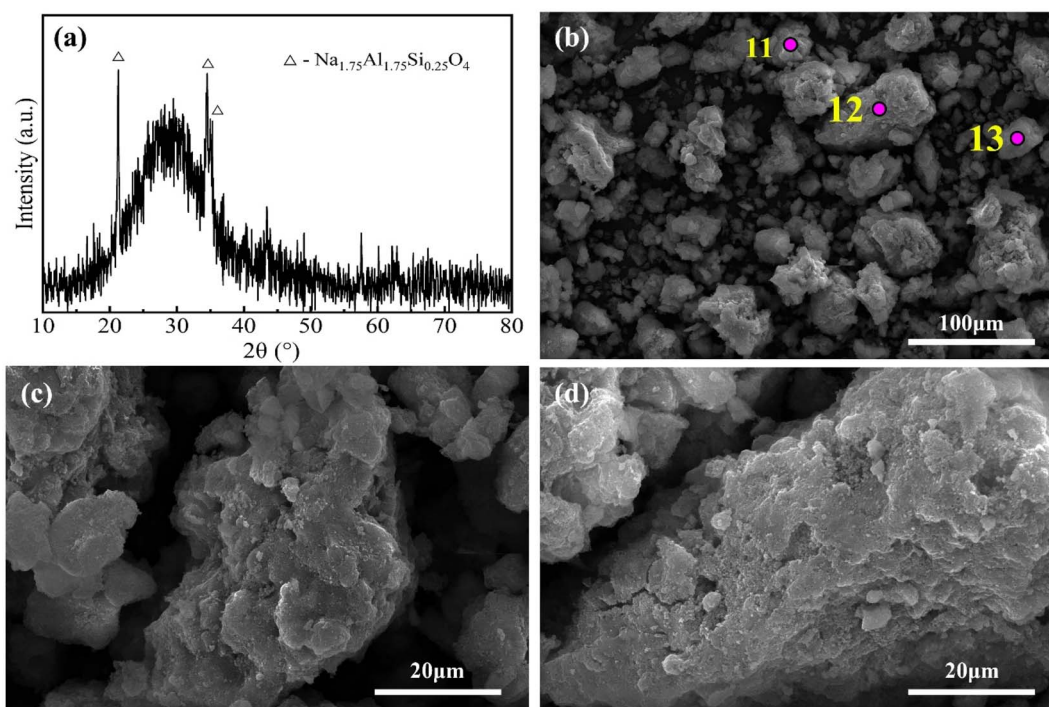
Fig. 9 XRD pattern (a) and SEM images (b–d) of the water leaching residue obtained at optimal sintering parameters.

Table 5 Elemental compositions of the water leaching residue particles from EDS analysis (wt%)

Element	O	Na	Al	Si	Ca	Ti	Fe
Spot 11	44.16	9.37	11.06	18.09	2.16	3	5.87
Spot 12	40.75	10.52	12.34	19.06	2.2	3.99	11.14
Spot 13	41.64	8.75	11.06	16.9	2.55	2.89	6.95
Average (11–13)	42.18	9.55	11.49	18.02	2.30	3.29	7.99
Standard deviation	1.77	0.90	0.74	1.08	0.21	0.61	2.78

3.3 Phase transformations

The phase transformations in the sintered samples and water leaching residues obtained at various sintering parameters were analyzed by XRD, and the results are shown in Fig. 7.

Fig. 7(a) shows the XRD patterns of the sintered samples obtained at different sintering temperatures. At 850 °C, the crystallographic phases in the sintered sample were primarily $Na_{1.95}Al_{1.95}Si_{0.05}O_4$ and $Na_{1.75}Al_{1.75}Si_{0.25}O_4$. In addition, trace amounts of α-Al_2O_3 and Na_2CO_3 were also present in the sintered sample, indicating that the reaction between bauxite and Na_2CO_3 had not yet fully occurred. As the sintering temperature increased to 950 °C, the diffraction peaks of $Na_{1.75}Al_{1.75}Si_{0.25}O_4$, α-Al_2O_3 and Na_2CO_3 weakened, while those of $Na_{1.95}Al_{1.95}Si_{0.05}O_4$ increased in intensity, indicating that $Na_{1.75}Al_{1.75}Si_{0.25}O_4$, α-Al_2O_3 and Na_2CO_3 reacted to form $Na_{1.95}Al_{1.95}Si_{0.05}O_4$. At 950 °C and above, only $Na_{1.95}Al_{1.95}Si_{0.05}O_4$ and $Na_{1.75}Al_{1.75}Si_{0.25}O_4$ were detected in the sintered samples, and the former was gradually converted into the latter with increasing temperature. According to the TGA/DSC

analysis (Fig. 4), the transformation of $Na_{1.95}Al_{1.95}Si_{0.05}O_4$ into $Na_{1.75}Al_{1.75}Si_{0.25}O_4$ was exothermic. Fig. 7(b) shows the XRD patterns of the water leaching residues corresponding to the sintered samples in Fig. 7(a). At 850 °C, only α-Al_2O_3 was detected in the water leaching residue. As the sintering temperature increased to 1050 °C, the diffraction peaks of α-Al_2O_3 weakened and disappeared, while those of $Na_{1.75}Al_{1.75}Si_{0.25}O_4$ arose and increased in intensity. At 950 °C and above, only $Na_{1.75}Al_{1.75}Si_{0.25}O_4$ were detected in the water leaching residues. In addition, an amorphous peak was present in where 2θ is in the range of 20–40°, indicating the presence of amorphous phase in the water leaching residues.

The XRD patterns of the sintered samples and water leaching residues obtained at different sintering times were shown in Fig. 7(c) and (d), respectively. The changes in the XRD patterns at 10–30 min presented similar trends to those at 850–950 °C in Fig. 7(a) and (b). When the sintering time prolonged from 30 min to 50 min, the XRD patterns had no obvious changes anymore.

The XRD patterns of the sintered samples obtained at different N/(A + S) were shown in Fig. 7(e). When N/(A + S) was 0.6, $Na_{1.75}Al_{1.75}Si_{0.25}O_4$, α-Al_2O_3 and $Na_{1.95}Al_{1.95}Si_{0.05}O_4$ were detected in the sintered sample, in which $Na_{1.75}Al_{1.75}Si_{0.25}O_4$ played a dominant role. As N/(A + S) increased from 0.6 to 1.4, $Na_{1.75}Al_{1.75}Si_{0.25}O_4$ and α-Al_2O_3 transformed into $Na_{1.95}Al_{1.95}Si_{0.05}O_4$ entirely. In addition, the diffraction peaks of Na_2CO_3 and $NaAlO_2$ arose at N/(A + S) of 1.2 and 1.4, respectively. The presence of Na_2CO_3 in the sintered samples suggested an overdosing of it. The XRD patterns of the water leaching residues corresponding to the sintered samples in Fig. 7(e) were shown in Fig. 7(f). When N/(A + S) was 0.6, $Na_{1.75}Al_{1.75}Si_{0.25}O_4$ and α-
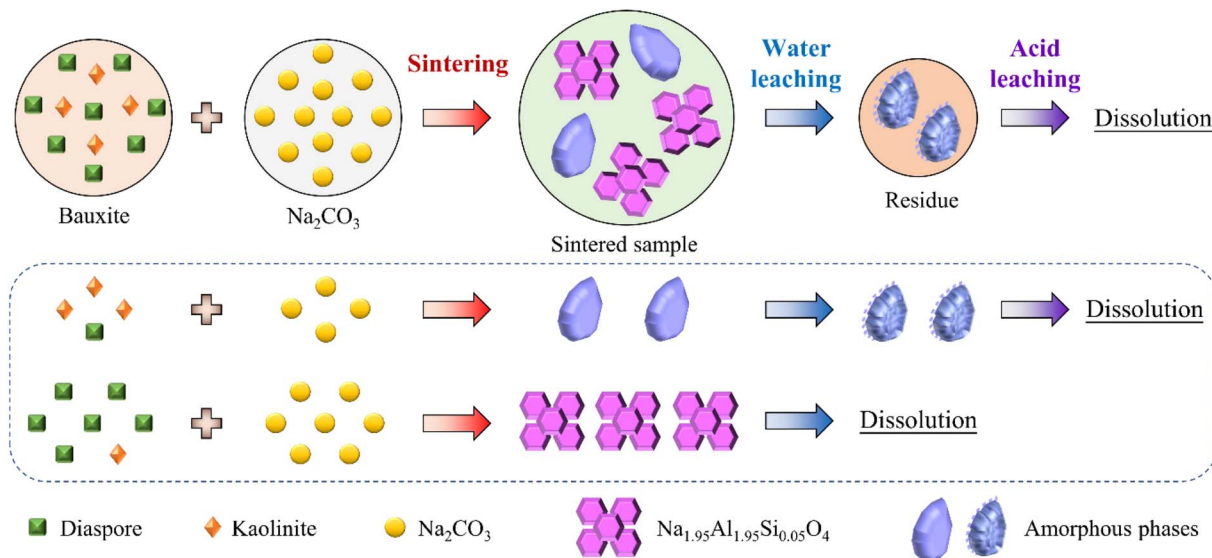
Fig. 10 Schematic diagram of the process mechanism at optimal sintering parameters.

Al_2O_3 were detected in the water leaching residue. As $N/(A + S)$ increased from 0.6 to 1.4, the diffraction peaks of $Na_{1.75}Al_{1.75}Si_{0.25}O_4$ and α-Al_2O_3 weakened and disappeared, leaving only those of amorphous phases.

Comparing the major phases in the sintered samples (Fig. 7(a), (c) and (e)) with those in the corresponding water leaching residues (Fig. 7(b), (d) and (f)), it can be known that Na_2CO_3, $Na_{1.95}Al_{1.95}Si_{0.05}O_4$ and $NaAlO_2$ were entirely dissolved during water leaching, while $Na_{1.75}Al_{1.75}Si_{0.25}O_4$ was partially dissolved, and α-Al_2O_3 was not dissolved. Therefore, the extraction of Al_2O_3 in water leaching process was primarily related to the formation and transformation of $Na_{2-x}Al_{2-x}Si_xO_4$ ($x = 0$, 0.05 and 0.25) in the sintered samples. According to Fig. 5, η_{A1} was relatively low when $Na_{1.75}Al_{1.75}Si_{0.25}O_4$ was dominant in the sintered samples, and significantly increased with the transformation of $Na_{1.75}Al_{1.75}Si_{0.25}O_4$ into

$Na_{1.95}Al_{1.95}Si_{0.05}O_4$. When $Na_{1.95}Al_{1.95}Si_{0.05}O_4$ was further converted into $NaAlO_2$, η_{A1} increased only slightly. In the water leaching process, few SiO_2 in the sintered sample was leached out with the dissolution of $Na_{1.75}Al_{1.75}Si_{0.25}O_4$ and $Na_{1.95}Al_{1.95}Si_{0.05}O_4$, while most of SiO_2 was left in the water leaching residue. After water leaching, α-Al_2O_3, $Na_{1.75}Al_{1.75}Si_{0.25}O_4$, and an amorphous phase were retained in the water leaching residues, where one of the latter two phases dominated. According to the experimental phenomena, the water leaching residues without α-Al_2O_3 was almost completely dissolved during acid leaching, indicating that $Na_{1.75}Al_{1.75}Si_{0.25}O_4$ and the amorphous phase have excellent acid solubility. As a result, almost all the remaining Al_2O_3 and SiO_2 in the water leaching residue were extracted, leading to high levels of η_{AT}, η_S and the purity of silica powder. In contrast, η_{AT} was lower when α-Al_2O_3 was present in the water leaching residue, indicating that α-Al_2O_3 was difficult
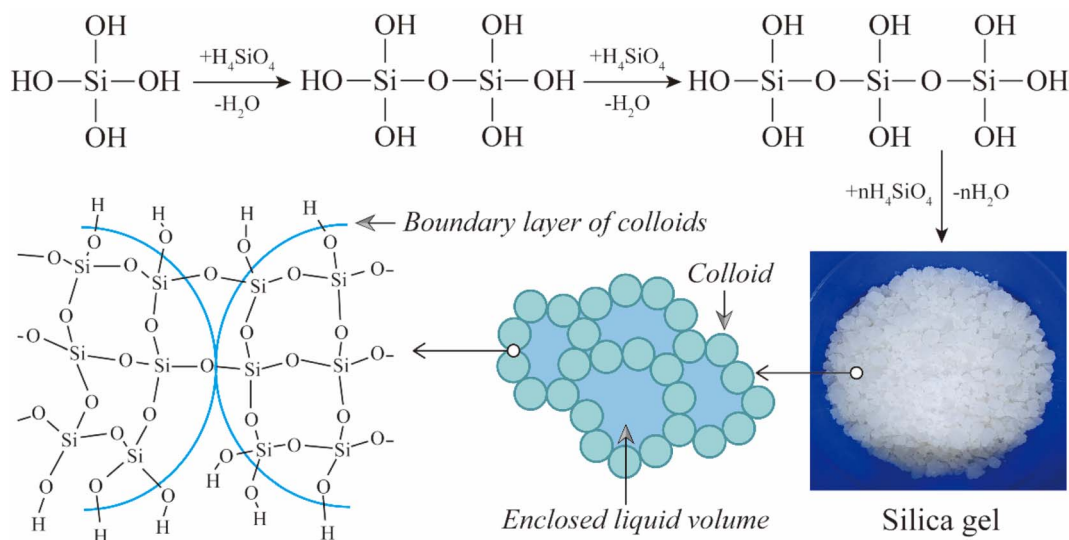

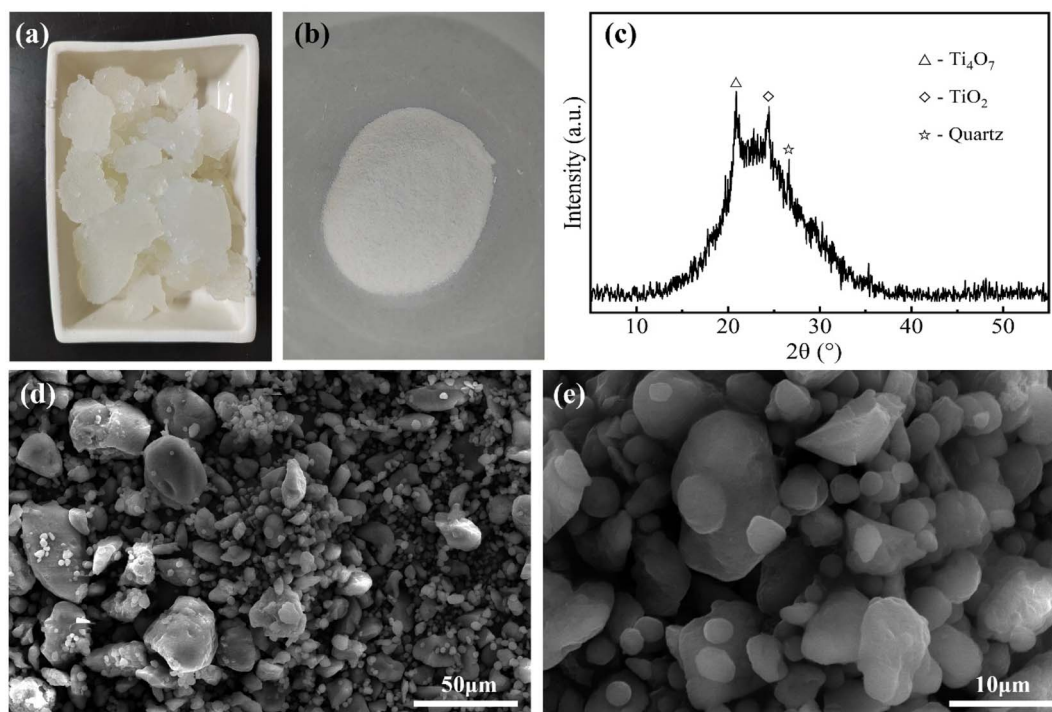Fig. 11 Diagram of the formation mechanism of silica gel.[43]

Fig. 12 Photographs of silica gel (a) and silica powder (b); XRD pattern (c) and SEM images (d and e) of silica powder.

to dissolve during acid leaching. As a result, the purity of silica powder was also lower.

The optimal sintering parameters (950 °C, 30 min and N/(A + S) = 1) were selected to compare the identified phases in Fig. 7 with the thermodynamic predictions of Fig. 3. The identified phases in the sintered sample were primarily $Na_{2-x}Al_{2-x}Si_xO_4$ (x = 0.05 and 0.25), which are $NaAlO_2$ solid solutions predicted by thermodynamics. In addition to the $NaAlO_2$ solid solutions, a liquid slag was also predicted by thermodynamics, which contained most of the SiO_2 in the $Na_2O–Al_2O_3–SiO_2$ system. The crystallinity of the sintered sample was calculated to be 80.3%, indicating the presence of an amorphous phase, which is the main Si-bearing phase in the sintered sample and corresponds to the liquid slag predicted by thermodynamics.

3.4 Micromorphology

In order to further reveal the process mechanism, the micromorphology of the sintered sample and water leaching residue obtained at optimal sintering parameters were observed and analyzed.

Fig. 8 shows the XRD pattern and SEM images results for the sintered sample. According to Fig. 8(b), the particles in the sintered sample could be divided into two groups. As shown in Fig. 8(c), the first kind of particles were loose and porous aggregates of fine lamellar crystals, which is favorable for water leaching. According to Fig. 8(a), the crystalline phase in the sintered sample was primarily $Na_{2-x}Al_{2-x}Si_xO_4$ (x = 0.05 and 0.25). Combined with the EDS results of spot 5–7 (Table 4), it could be concluded that the first kind of particles mostly consisted of $Na_{2-x}Al_{2-x}Si_xO_4$ (x = 0.05 and 0.25). As shown in Fig. 8(d), the second kind of particles were in the form of dense blocks with smooth surfaces and numerous microscopic pores inside. The micromorphology indicated that the second kind of particles were amorphous, which verifies the presence of an amorphous phase in the sintered sample. According to Table 4, the second kind of particles (spot 8–10) contained less Na, Al and more Ca, Ti, Fe compared to the first kind of particles (spot 5–7). The average A/S of these two kinds of particles were 4.23 and 2.61, respectively, while that of the sintered sample was 3.71. Based on the difference in A/S, the proportion of the first

Table 6 Comparison between the novel process and the lime-soda sintering process

Process	Sintering parameters	Recovery efficiency			Emission of residue
		Al_2O_3	SiO_2	Fe_2O_3	
The lime-soda sintering process	1250–1350 °C C/S = 2, N/A = 1	88–92%	—	—	>1.5 t per t-Al_2O_3
The novel process	950 °C N/(A + S) = 1	97.7% (84.2% for alumina, 13.5% for PAFS)	86.4%	95.9%	0

and second kinds of particles was calculated to be about 68% and 32%, respectively.
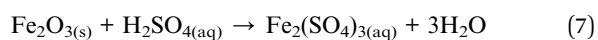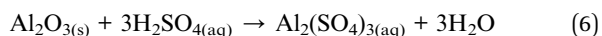
Fig. 9 shows the XRD pattern and SEM images of the water leaching residue obtained at optimal sintering parameters. According to Fig. 9(a), the water leaching residue was primarily composed of amorphous phases. As shown in Fig. 9(b)–(d), the amorphous particles were primarily massive, with rough surfaces and numerous dissolution pores, which was inferred to be the result of partial dissolution and secondary reactions of the amorphous phase particles in the sintered sample during water leaching. The EDS results of the amorphous particles in the sintered sample (Table 4) and water leaching residue (Table 5) show that the contents of Na and Al decreased after water leaching, while those of Si, Ca, Ti and Fe increased relatively, further confirming the above inference. As a result, the A/S of the amorphous particles decreased to 0.56, which was similar to that of the water leaching residue (0.58). In addition, the particles in the water leaching residue have a size of less than 100 μm and a porous structure, which favors acid leaching.

3.5 Discussion of the mechanism and advantages of the novel process

Based on the above analysis results, the phase transformations of the Al- and Si-bearing minerals during sintering and leaching were revealed. In addition, the formation mechanism and application of silica gel were discussed.

In this study, diaspore and kaolinite are the main Al- and Si-bearing minerals in the high-silica bauxite, respectively. In the sintering process, diaspore and kaolinite were primarily converted into $Na_{2-x}Al_{2-x}Si_xO_4$ ($x = 0$, 0.05 and 0.25) and an amorphous phase by fully reacting with sufficient Na_2CO_3. In the water leaching process, $Na_{2-x}Al_{2-x}Si_xO_4$ ($x = 0$, 0.05 and 0.25) dissolves completely or partially depending on the x value, while the amorphous phase partially dissolves and undergoes some secondary reactions. The residual amorphous phase and $Na_{2-x}Al_{2-x}Si_xO_4$ ($x = 0.25$) formed the main body of the water leaching residue and were almost completely dissolved in the subsequent acid leaching process. If the dosage of Na_2CO_3 is insufficient or the sintering reaction does not fully occur, a part of diaspore would be dehydroxylated to form α-Al_2O_3, which is insoluble in both the water leaching and acid leaching processes. Fig. 10 shows the proposed mechanism at optimal sintering parameters.

According to Table 3, the chemical composition of the water leaching residue was dominated by SiO_2, Al_2O_3 and Fe_2O_3, which underwent the following reactions during acid leaching.[41,42]

$$M_2SiO_{4(s)} + 2H_2SO_{4(aq)} \rightarrow H_4SiO_{4(aq)} + 2MSO_{4(aq)} \quad (5)$$

$$Al_2O_{3(s)} + 3H_2SO_{4(aq)} \rightarrow Al_2(SO_4)_{3(aq)} + 3H_2O \quad (6)$$

$$Fe_2O_{3(s)} + H_2SO_{4(aq)} \rightarrow Fe_2(SO_4)_{3(aq)} + 3H_2O \quad (7)$$

Accordingly, the compositions of the acid leaching solution were dominated by H_4SiO_4, $Al_2(SO_4)_3$, and $Fe_2(SO_4)_3$. H_4SiO_4 will gradually polymerize in the acid leachate,

forming dimers, trimers, cyclic oligomers and up to silica gels,[43,44] as shown in Fig. 11. Pure silica gel was obtained using the method described in Section 2.2, as shown in Fig. 12(a). The silica gel has excellent water absorbing properties, containing 90–95% water, which can be processed as a water retention agent, desiccant, or absorbent. The silica powder (Fig. 12(b)) obtained by drying silica gel has a high purity of 87–90%, which is primarily amorphous according to Fig. 12(c). As shown in Fig. 12(d) and (e), the amorphous silica particles are primarily layered and thus have a specific surface area of up to $\sim$406 m^2 g^{-1}. Therefore, the silica gel can also be used as a raw material for the production of silica-based products. After separating out silica gel, the remaining solution had $Al_2(SO_4)_3$ and $Fe_2(SO_4)_3$ as the main components, which can be used to produce PAFS.[35]

The above process realizes the comprehensive utilization of high silica bauxite and has obvious advantages compared with the traditional lime-soda sintering process, as shown in Table 6. First, lime is not introduced into the sintering process, reducing the material flow and improving the production efficiency. Second, the sintering temperature is reduced from 1250–1350 °C to 950 °C, resulting in lower sintering energy consumption. Third, SiO_2 and Fe_2O_3 are also extracted and utilized with high levels of recovery in addition to Al_2O_3. Fourth, residue is fully utilized without discharge.

4 Conclusions

The extraction of Al_2O_3 and SiO_2 from high-silica bauxite was realized by sintering with N_2CO_3 followed by two-step leaching with water and acid. During the sintering of bauxite with N_2CO_3, diaspore and kaolinite were transformed into α-Al_2O_3, $Na_{2-x}Al_{2-x}Si_xO_4$ ($x = 0$, 0.05 and 0.25) and an amorphous phase. In the subsequent two-step leaching processes, α-Al_2O_3 was insoluble, while the other two phases were almost completely dissolved. The formation of α-Al_2O_3 could be avoided by adjusting sintering parameters. The optimal sintering parameters were determined experimentally to be sintering temperature of 950 °C, sintering time of 30 min, and N/(A + S) of 1. Under these conditions, $\sim$97% of Al_2O_3 and $\sim$86% of SiO_2 were extracted for the production of alumina, PAFS and silica gel. The purity of silica gel was positively correlated with the total recovery efficiency of Al_2O_3. The dried silica gel reached a purity of $\sim$88% at optimal sintering parameters. These findings suggest an idea for the comprehensive utilization of high-silica bauxite and the minimization of residue.

Conflicts of interest

There are no conflicts to declare.

Acknowledgements

References

1 N. Zhang, A. V. Nguyen and C. Zhou, *Adv. Colloid Interface Sci.*, 2018, **254**, 56–75.

2 P. Smith, *Hydrometallurgy*, 2009, **98**, 162–176.

3 Z. Wu, H. Lv, M. Xie, L. Li, H. Zhao and F. Liu, *Ceram. Int.*, 2022, **48**, 18676–18686.

4 X. Pan, H. Wu, H. Yu and S. Bi, *Hydrometallurgy*, 2020, **197**, 105469.

5 N. Kawashima, L. Shi, N. Xu, J. Li and A. R. Gerson, *Hydrometallurgy*, 2016, **159**, 75–86.

6 B. Gibson, D. G. Wonyen and S. C. Chelgani, *Miner. Eng.*, 2017, **114**, 64–73.

7 Y. Wu, X. L. Pan, Y. J. Han and H. Y. Yu, *Trans. Nonferrous Met. Soc. China*, 2019, **29**, 2627–2637.

8 Y. Xu, J. Li, C. Chen, Y. Lan and L. Wang, *JOM*, 2020, **72**, 2705–2712.

9 X. B. Li, H. Y. Wang, Q. S. Zhou, T. G. Qi, G. H. Liu, Z. H. Peng and Y. L. Wang, *Trans. Nonferrous Met. Soc. China*, 2019, **29**, 416–423.

10 Q. Wang, X. F. Sheng, L. Y. He and Y. Shan, *Miner. Eng.*, 2018, **128**, 179–186.

11 G. Lü, T. Zhang, X. Zhu, C. Zheng, Y. Wang, W. Zhang and Z. Zhang, *Chin. J. Chem. Eng.*, 2019, **27**, 1965–1972.

12 Y. Wang, T. Zhang, G. Lyu, L. Ma and W. Zhang, *J. Cleaner Prod.*, 2021, **290**, 125828.

13 C. Liu, S. Ma, S. Zheng, Y. Luo, J. Ding, X. Wang and Y. Zhang, *Hydrometallurgy*, 2018, **175**, 224–231.

14 S. N. Wang, S. L. Zheng and Y. Zhang, *Chin. J. Process Eng.*, 2007, **7**, 967–972.

15 A. Alp and A. O. Aydin, *Can. Metall. Q.*, 2002, **41**, 41–46.

16 J. Pei, X. Pan, Y. Zhang, H. Yu and G. Tu, *J. Environ. Chem. Eng.*, 2021, **9**, 106754.

17 T. Le, S. Ju, L. Lu, J. Peng, L. Zhou and S. Wang, *Hydrometallurgy*, 2017, **169**, 124–134.

18 A. B. ElDeeb, V. N. Brichkin, M. Bertau, Y. A. Savinova and R. V. Kurtenkov, *Appl. Clay Sci.*, 2020, **196**, 105771.

19 Y. J. Xu, H. X. Xin, H. M. Duan, Y. D. Li, Y. Wu, J. Lin and Y. C. Zhai, *J. Cent. South Univ.*, 2022, **29**, 22–31.

20 D. Tian, X. Y. Shen, Y. C. Zhai, P. Xiao and P. Webley, *J. Iron Steel Res. Int.*, 2019, **26**, 578–584.

21 D. Valeev, A. Shoppert, D. Dogadkin, T. Romashova, T. Kuz'mina and C. Salazar-Concha, *Hydrometallurgy*, 2023, **215**, 105994.

22 Y. Zhang, J. Zhang, L. Wu, L. Tan, F. Xie and J. Cheng, *J. Hazard. Mater.*, 2021, **404**, 124044.

23 Y. Zhao, Y. Zheng, H. He, Z. Sun and A. Li, *J. Environ. Chem. Eng.*, 2021, **9**, 104770.

24 T. S. Barry, T. Uysal, M. Birinci and M. Erdemoğlu, *Min., Metall., Explor.*, 2019, **36**, 557–569.

25 S. Ma, Z. Wen, J. Chen and S. Zheng, *Miner. Eng.*, 2009, **22**, 793–798.

26 J. Y. Ma, Z. B. Li and Q. G. Xiao, *AIChE J.*, 2012, **58**, 2180–2191.

27 W. Liu, J. Yang and B. Xiao, *Int. J. Miner. Process.*, 2009, **93**, 220–231.

28 Y. Li, X. Pan, Z. Lv, H. Wu and H. Yu, *Miner. Eng.*, 2022, **187**, 107805.

29 Y. Xu, C. Chen, Y. Lan, L. Wang and J. Li, *J. Mater. Res. Technol.*, 2020, **9**, 7418–7426.

30 Y. Wang, T. Zhang, Y. Zhang, G. Lyu and W. Zhang, *Miner. Eng.*, 2019, **138**, 139–147.

31 G. Power, M. Grafe and C. Klauber, *Hydrometallurgy*, 2011, **108**, 33–45.

32 X. Liu, Y. Han, F. He, P. Gao and S. Yuan, *J. Hazard. Mater.*, 2021, **420**, 126542.

33 P. S. Reddy, N. G. Reddy, V. Z. Serjun, B. Mohanty, S. K. Das, K. R. Reddy and B. H. Rao, *Waste Biomass Valorization*, 2021, **12**, 1185–1217.

34 Y. Wang, T.-a. Zhang, G. Lyu, F. Guo, W. Zhang and Y. Zhang, *J. Cleaner Prod.*, 2018, **188**, 456–465.

35 J. Chang, A. Pan, Y. Ma, Y. Sun and S. Hu, *Minerals*, 2023, **13**, 105.

36 J. Chang, A. Pan, Y. Ma, Y. Sun, S. Hu and K. Li, *Metall. Res. Technol.*, 2022, **119**, 114.

37 Y. Sun, A. Pan, Y. Ma, J. Chang, K. Li and S. Hu, *Miner. Eng.*, 2022, **187**, 107782.

38 T. Le, S. H. Ju, A. V. Ravindra, X. T. Li and Q. Wang, *JOM*, 2019, **71**, 831–837.

39 C. Dessemond, G. Soucy, J.-P. Harvey and P. Ouzilleau, *Minerals*, 2020, **10**, 519.

40 A. Kosminski, D. P. Ross and J. B. Agnew, *Fuel Process. Technol.*, 2006, **87**, 1051–1062.

41 G. Hu, H. Tang, D. He, W. Sun and L. Wang, *Miner. Eng.*, 2021, **173**, 107180.

42 H. Tanvar and B. Mishra, *Sustainable Mater. Technol.*, 2022, **33**, e00466.

43 G. Alkan, B. Yagmurlu, S. Cakmakoglu, T. Hertel, Ş. Kaya, L. Gronen, S. Stopic and B. Friedrich, *Sci. Rep.*, 2018, **8**, 5676.

44 D. Voßenkaul, A. Birich, N. Müller, N. Stoltz and B. Friedrich, *J. Sustain. Metall.*, 2017, **3**, 79–89.

© 2023 The Author(s). Published by the Royal Society of Chemistry